Spectrochimica Acta Part A: Molecular and Biomolecular Spectroscopy 234 (2020) 118272

Contents lists available at ScienceDirect

Spectrochimica Acta Part A: Molecular and Biomolecular Spectroscopy

journal homepage: www.elsevier.com/locate/saa

Cerium doped magnetite nanoparticles for highly sensitive detection of metronidazole via chemiluminescence assay

Yasin Orooji [a,b], Mahsa Haddad Irani-nezhad [c], Ramin Hassandoost [c], Alireza Khataee [c,d,e,*], Shima Rahim Pouran [f], Sang Woo Joo [g,*]

[a] College of Materials Science and Engineering, Nanjing Forestry University, No. 159, Longpan Road, Nanjing, 210037, Jiangsu, People's Republic of China
[b] Co-Innovation Center of Efficient Processing and Utilization of Forest Resources, Nanjing Forestry University, Nanjing 210037, China
[c] Research Laboratory of Advanced Water and Wastewater Treatment Processes, Department of Applied Chemistry, Faculty of Chemistry, University of Tabriz, 51666-16471 Tabriz, Iran
[d] Department of Environmental Engineering, Gebze Technical University, 41400 Gebze, Turkey
[e] Institute of Research and Development, Duy Tan University, Da Nang 550000, Viet Nam
[f] Department of Biology, Faculty of Science, University of Mohaghegh Ardabili, P.O. Box 179, Ardabil, Iran
[g] School of Mechanical Engineering, Yeungnam University, Gyeongsan 712-749, South Korea

ARTICLE INFO

Article history:
Received 28 January 2020
Received in revised form 14 March 2020
Accepted 15 March 2020
Available online 17 March 2020

Keywords:
Antibiotics detection
Chemiluminescence
Human plasma
Magnetic sensor
Metronidazole

ABSTRACT

Cerium doped magnetite nanoparticle (CDM) was synthesized via a co-precipitation method and used as the co-reactant of luminol-$K_3Fe(CN)_6$ chemiluminescent system. The physical-chemical features of CDM were studied by XPS, XRD, HRTEM, FESEM, VSM, BET, and FTIR analyses. This simple and highly sensitive nanoprobe enabled the determination of minor concentrations of metronidazole (MNZ). Owing to the quenching efficacy of MNZ in the studied chemiluminescence system, a linear range of 3.47×10^{-6}-9.37×10^{-5} mol/L was obtained with a limit of detection of 3.91×10^{-7} mol/L. This biosensor was used for MNZ detection in human serum samples, which was highly efficient. The outcomes of this study give credit to the proposed biosensor to be applied for detection of MNZ in biological samples.

1. Introduction

Currently, detecting the signals of the targeted analytes such as antibiotics, toxins, proteins, glucose, hormones, and DNA is facilitated by biosensors. These devices, with their unique features such as the early diagnosis of diseases by detecting analytes and biomarkers from human blood, urine, and saliva, are at the forefront of attention. Detecting the signals of different nature such as capacitance, electric potential, impedance, current, and/or light intensity is the basis of biosensors operation [1]. Chemiluminescence (CL), a method that requires no light source, is used to detect the target analyte based on the produced photons during some specific chemical reactions. This property makes CL more applicable than the widely used fluorescence (FL) technique [2,3]. The other advantages of CL over FL are being appropriate in small-sized systems and for miniaturization, facile instrumentation and operation, and a low limit of detection with a wide linear range for quantifying various analytes [4].

Nowadays, inspiring applications of sensors propel scientists to integrate them with nanotechnology. Given that the intrinsic CL illumination of luminol and its low quantum yield can be enhanced by various compounds such as nanoparticles, metal oxides, metal ions, and enzymes [5]. Hence, one of the appealing research interests of scientists is to modify nanomaterials in order to advance some particular physical-chemical properties of them [6]. It has been demonstrated that the surface defects, chemical composition, crystal structure, size and surface properties are of critical factors of engineered nanomaterials for sensing applications [7]. Rare earth metal doped nanomaterials have shown exceptional chemical, physical, and mechanical properties, which are imperative for analytical approaches [8].

Magnetite (Fe_3O_4, MAG) has been frequently used in several applications such as catalysis, sensor, nanofluid, and electronics, owing to its unique properties including low toxicity, narrow bandgap, easy modification, and superparamagnetism [9,10]. Both chemical and physical properties of MAG nanoparticles (NPs), such as morphology, particle size, magnetic behavior, and surface functionalization have great effects on the enhancement of detection sensitivity [11,12]. Zhang et al. [13] fabricated an innovative and intrinsically selective MAG-based chemosensor for simultaneous detection of 2,4-dichlorophenoxyacetic acid, ethoprophos, profenofos, and dylox. In their study, the effects of

* Corresponding authors.
E-mail addresses: alirezakhataee@duytan.edu.vn, a_khataee@tabrizu.ac.ir (A. Khataee), swjoo@yu.ac.kr (S.W. Joo).

https://doi.org/10.1016/j.saa.2020.118272
1386-1425/

the surface modification of MAG NPs were assessed on the adjustable CL switching. In another work, Shen et al. [14] reported the usage of the zinc ferrite ($ZnFe_2O_4$) in electro-chemiluminescence immune-sensor for detection of carcinoembryonic antigen. For this purpose, $ZnFe_2O_4$@Au and CdTe-graphene combined with anti-bodies to form a sandwich-like structure and enhanced the electrochemiluminescence efficiency. Recent studies reported the fabrication of a number of probes using modified MAG chemiluminescent sensors such as silanized magnetic graphene, oxide-molecularly imprinted polymer [15] or β–cyclodextrins-$CoFe_2O_4$ magnetic NPs [16]. However, either their linear range was low or the detection limit was high. These limitations motivated us to modify MAG in an effort to enhance its properties for sensor-based applications.

One method to increase MAG catalytic activity is to be doped with rare earth metals such as Terbium [17], Europium [18], and Lanthanide [19]. In this method, several factors such as the particle size, amount of the incorporation, and valence states of metals have influential effects on the catalytic activity of MAG NPs [20]. Moreover, the metal cation's distribution through the octahedral and tetrahedral sites of the MAG crystal lattice plays a big role in its catalytic activity. This is because the octahedral sites of MAG are more catalytically active due to their exposition on the surface of MAG spinel crystallites [21]. Notably, the substitution or incorporation of rare earth metals changes the surface properties of MAG such as specific surface area and surface functional groups (e.g. hydroxyl groups) to some extent. From the earth rare metals, cerium has been studied by many researchers because of its Ce^{3+}/ Ce^{4+} redox property [22]. The Ce^{3+}/Ce^{4+} redox pair have shown considerable synergistic effects on the catalytic activity of Fe-bearing composites. Basically, doping of Ce ions with MAG enhances the electron transfer process among the Ce^{3+}/Ce^{4+} and Fe^{2+}/Fe^{3+} redox pairs and elevates the catalytic activity of MAG via the oxidation-based reactions [23].

Metronidazole (MNZ) tablets have been used as an antibiotic for the treatment of giardiasis, trichomoniasis, dental infection, amoebiasis, and acute ulcerative gingivitis [24]. Though the explicit toxicity of metronidazole has still remained an issue, some of the side effects such as ataxia, peripheral neuropathy, and seizures have been identified after MNZ accumulation in human body and wildlife. On the other hand, due to its high solubility in water and non-biodegradability, the precise detection and removal of MNZ is technically challenging [25].

In this study, a novel and sensitive CL system were developed using cerium doped magnetite nanoparticles (CDM). It was inspected that the $Fe_{2.8}Ce_{0.2}O_4$ NPs had the highest enhancement effects than those of Fe_3O_4, CeO_2, and ceria mechanically doped magnetite (CMDM) nanoparticles on the luminol-$K_3Fe(CN)_6$ CL system. The CL intensity of luminol, which was reacted with a weak oxidant, $K_3Fe(CN)_6$, in a continuous flow injection was examined when undergone a catalytic reaction by CDM nanoparticles. The fabricated sensor was used to determine MNZ in human plasma and spiked water samples. Moreover, the effect of the MNZ analogues was investigated on the designed CL system. Besides, the possible mechanism of the proposed CL system was investigated.

2. Experiments

2.1. Reagents

Metronidazole ($C_6H_9N_3O_3$, 99%) was purchased from Jalinous pharmaceutical company (Iran). Lead (II) nitrate ($Pb(NO_3)_2$, ≥99.0%), copper(II) chloride ($CuCl_2$, 97%), potassium bromide (KBr, ≥99%), cerium nitrate hexahydrate ($Ce(NO_3)_3.6H_2O$, 99%), cobalt (II) chloride ($CoCl_2$, ≥98%), sodium hydroxide (NaOH, ≥98%), magnesium chloride ($MgCl_2$, ≥98%), iron (II) chloride tetrahydrate ($FeCl_2.4H_2O$, 99.99%), Nickel(II) sulfate ($NiSO_4$, ≥98%), iron(II) sulfate heptahydrate ($FeSO_4.7H_2O$, ≥99%), sodium nitrate ($NaNO_3$, ≥99%), hydrazine (N_2H_4, 65%), trisodium phosphate (Na_3PO_4, 96%), hydrochloric acid (HCl, 37%), zinc nitrate ($Zn(NO_3)_2$, 98%), urea ($CO(NH_2)_2$, ≥98%), sodium acetate ($NaCH_3COO$, ≥99%), acetone ($OC(CH_3)_2$, ≥99.5%), calcium chloride ($CaCl_2$, ≥97%), sodium sulfate (Na_2SO_4, ≥97%), sodium carbonate (Na_2CO_3, ≥99%), pure ethanol (C_2H_5OH, 95%), luminol ($C_8H_7N_3O_2$, 97%), and potassium ferricyanide ($K_3Fe(CN)_6$, 99%) were acquired from Merck (Germany). Also, valine ($C_5H_{11}NO_2$, ≥98%), starch ($(C_6H_{10}O_5)_n$ -(H_2O), ≥97%), alanine ($C_3H_7NO_2$, ≥98%), glucose ($C_6H_{12}O_6$, ≥99.5%), and lactose ($C_{12}H_{22}O_{11}$, ≥99%) were purchased from Aladdin (China). All of the chemicals used in this work were of analytical grade without further purification and used as obtained.

2.2. Apparatus

The chemical structure and morphology of the synthesized nanoparticles were determined by the X-ray photoelectron spectrometer (XPS, Thermo Scientific, K-Alpha, UK), X-ray diffraction (XRD, PW1730, Philips, the Netherlands, under 0.15406 nm of Cu-Kα radiation at current and accelerating voltage of 40 mA, 45 kV), Cs-corrected high-resolution transmission electron microscopy (HRTEM) images 200 kV (JEM-2200FS, JEOL, Japan, working at 200 kV), field emission scanning electron microscopy (FESEM) micrographs (Tescan Mira3 microscope, Czech Republic), vibrating sample magnetometer (VSM, Lakeshore Cryotronics, 7400 Series, USA), Brunauer-Emmett-Teller (BET, Belsorp Mini II, Japan, determined by nitrogen adsorption/desorption isotherms at 77 K), and Fourier transform infrared spectrometer (FTIR, Bruker Tensor 27, Germany). Moreover, for the chromatographic analysis, an HPLC system (Smartline 1000 Knauer, Germany) equipped with a C18 column and UV detector was used. To study the mechanism of the action of CDM nanoparticles, UV–Vis absorption spectra (S2000 spectrophotometer, WPA Lightwave, England) were recorded.

2.3. Synthesis of nanoparticles

As reported earlier [26], for the synthesis of Fe_3O_4, MAG, Argon bubbling was used to deoxygenate the aqueous solution. Then, in a three-neck flask, an acidic solution containing 0.9 mol/L of iron (II) chloride tetrahydrate was dissolved in 1.2 mol/L of hydrochloric acid to prepare 0.90 mol/L of Fe^{2+}. After that, 1 mL of hydrazine was added and pH was adjusted under 1.0 to prevent oxidation of Fe^{2+} and hydroxide precipitation. In the next step, the solution was boiled up to 100 °C and a basic solution containing sodium nitrate (0.90 mol/L) and sodium hydroxide (4.0 mol/L) with equal volumes was added slowly into the Fe^{2+} acidic solution. Then, while the mechanical stirring at 500 rpm for 2 h, the reaction was adjusted at 90 °C with Argon flux passing through. After 2 h, when the reaction completed, the solution was cooled to room temperature. The synthesized MAG was reaped by an external magnet and 10 min centrifugation at 3500 rpm and washed for 4–5 times with ethanol and boiling DI water. Then, MAG was collected via an external magnet and dried in a vacuum oven for 24 h at 100 °C. Finally, the MAG was finely powdered and filtered through a 200-mesh screen.

Production of CDM, $Fe_{2.8}Ce_{0.2}O_4$, was exactly similar to the MAG synthesis, with one difference: the acidic solution was produced by the 0.90 mol/L total concentration of the cerium and iron cations prepared from 2.60 g of $Ce(NO_3)_3 \cdot 6H_2O$ and 16.85 g of $FeCl_2 \cdot 4H_2O$ dissolved in 1.2 mol/L of HCl. The schematic of CDM NPs synthesis is shown in Scheme 1. The synthesis of ceria and CMDM NPs are provided in the Supplementary data (S1 and S2).

2.4. Preparation of samples

2.4.1. Preparation of the stock and working solutions

The weight of MNZ commercial tablets (five pieces) was measured and then grounded in a mortar. Next, a weight equal to 10 mg of MNZ

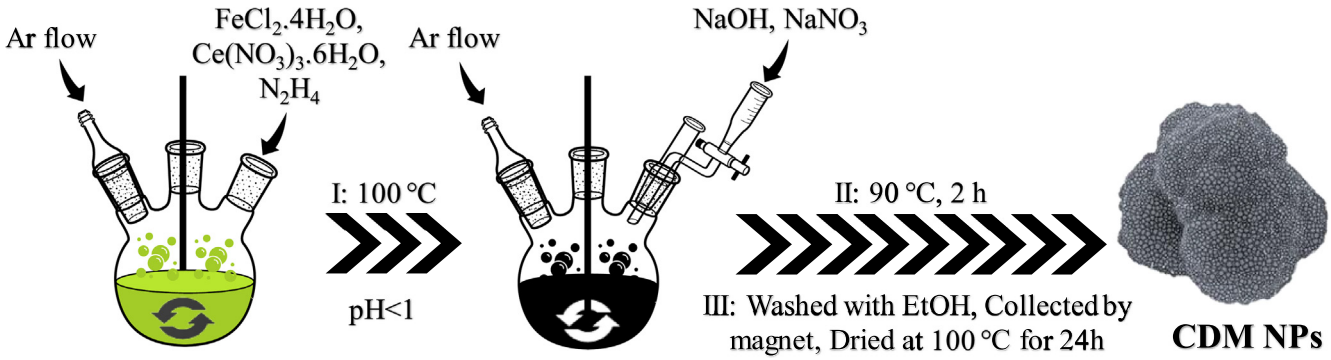

Scheme 1. The schematics of synthesis of CDM NPs.

was scaled and dissolved in double-distilled water (DDW). Whatman no. 42 filter paper was used to filter the resultant solution of which was diluted with DDW to prepare 5.84×10^{-4} mol/L MNZ stock solution. The serial dilution of the as-prepared MNZ stock solution gave rise to the working solutions.

2.4.2. Preparation of the calibration standards and quality control samples

One mL of each pre-known MNZ working solution was added to drug-free human plasma (10 mL) to prepare eight MNZ calibration standards other than zero, varying from 3.47×10^{-6} mol/L to 9.73×10^{-5} mol/L. A similar method was used to prepare the quality control samples (QC) at three concentration ranges including low, medium and high concentrations of MNZ (6.92×10^{-6}, 3.39×10^{-5} and 8.20×10^{-5} mol/L).

2.5. MNZ determination procedure

The schematic of the flow injection CL (FI-CL) system, employed for the detection of MNZ using luminol-$K_3Fe(CN)_6$ reaction catalyzed by CDM is displayed in Scheme 2. The setup featured polytetrafluoroethylene (PTFE) tubes (inner diameter of 1.0 mm), peristaltic pump, six-port valve, mixing tube, Y-shaped glassy connecter, luminometer detector, and a computer. Luminol solution (10^{-3} mol/L), alone or together with CDM (10^{-4} mol/L) and metronidazole (via line *c*), NaOH solution (1.5 mol/L, via line *d*), DI water (as carrier, via line *a*), and $K_3Fe(CN)_6$ solution (0.05 mol/L, as oxidant via line *b*) was pumped into the FI-CL system. The *c* and *d* solutions were combined by a blender tube (PTFE), and then, 100 μL of the resulted solution was injected into the carrier and a premixing was accomplished with an oxidant current in a Y-shaped glassy connecter, and finally, the blend was transferred into the flow cell. The CL emission peak resulted from the chemical reactions was steadily monitored in a computer connected to the luminometer (FB12 luminometer, Bad Wildbad, Germany).

2.6. Preparation of real samples

The real samples were prepared via modified methods. No pretreatment step was carried out for the tap water before analyzing. To prepare river water samples, the freshly sampled water was filtered through 0.45 μm polyamide membrane filter to eliminate the suspended solids and then stored in a refrigerator at 4 °C under dark condition. The samples were kept and used no longer than one week. Before analyses, different volumes of the standard solution of MNZ (5.84×10^{-4} mol/L) were mixed with 30 mL of water samples and diluted with DDW up to 50 mL.

For measuring MNZ in human plasma, it was procured from an Iranian Blood Transfusion Center (Tabriz, Iran). The only pretreatment step employed for human serum samples was deproteinization using nitric acid without any extraction course. The spiked samples were prepared by spiking pre-known values of MNZ into the serum (1.0 mL), following the addition of nitric acid (5.0 mL) into each sample and centrifugation for 15 min at 3000 rpm. The protein-free supernatant (2.5 mL) was diluted with DDW up to 50 mL.

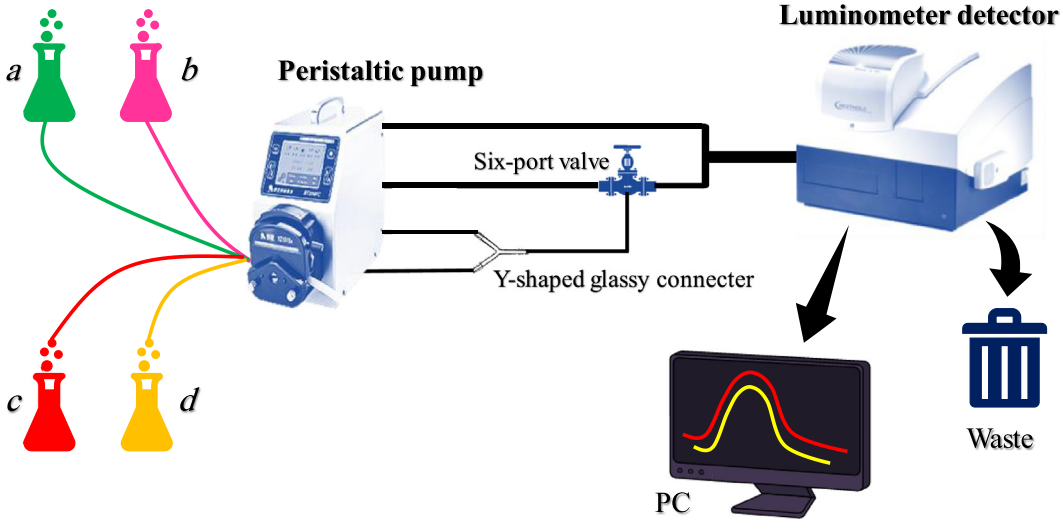

Scheme 2. The schematics of CL set-up.

3. Results and discussion

3.1. Characterization of nanoparticles

From the FESEM images depicted in Fig. 1a–c, the uniform spherical shape of MAG NPs with an average diameter of 10–16 nm can be observed. Fig. 1 (b and c) shows that the cerium doping of magnetite did not have a significant effect on the shapes and sizes of CDM and CMDM NPs [27]. For more information, FESEM images of the so-synthesized ceria NPs are displayed in Fig. S1. The HRTEM images (Fig. 1d,e) of nanoparticles indicated that both CDM and CMDM NPs were in the octahedral shape, which is regarded as the signature structure of MAG NPs. The d-spacing fringes of CDM NPs (Fig. 1d) were figured out to be 0.251 nm and 0.293 nm, which can be attributed to the (311) and (220) planes of MAG. Besides, for CMDM NPs (Fig. 1e). the characteristic lattice fringes of 0.249, 0.268, 0.292, and 0.313 nm were well-matched with the planes of MAG (311), ceria (200), MAG (220), and ceria (111), respectively [28].

The purity of the phase structure and crystallinity of the prepared MAG, CDM, and CMDM were studied by XRD patterns. As displayed in Fig. 1f, all the samples were quite consistent with the pattern of pure MAG (JCPDS File No.19–629) [29]. However, because of the low amounts of Ce and ceria in CDM and CMDM samples, the pure MAG pattern prevailed in the XRD patterns of CDM and CMDM. Furthermore, the XRD pattern of ceria is in good agreement with the cubic fluorite lattice structure of pure ceria (JCPDS File No.34-0394) as depicted in Fig. S2.

The chemical composition of the near-surface elements and their relative valance states were investigated by XPS analysis. The XPS survey scan of CDM sample is shown in Fig. S3. Moreover, Fig. 2, shows the HRXPS spectra of O 1s, Ce 3d, and Fe 2p that were used to identify the valance states of iron, cerium, and oxygen elements in the CDM sample. The O 1 s spectrum can be deconvoluted to three characteristic peaks at 529.32 eV (lattice O binding of Fe_3O_4), and the peaks at 530.03 eV and 531.25 eV energies, which are attributed to the lattice binding of oxygen with Ce ions and exterior hydroxyl radicals, respectively [30]. In the Ce 3d spectrum, the deconvoluted peaks at the binding energies of 903.77 and 885.27 eV are attributed to the Ce^{3+} $3d_{3/2}$ and Ce^{3+} $3d_{5/2}$, respectively. The peaks located at the binding energies of 916.65, 907.09, 900.99, 898.45, 888.74, and 882.11 eV are corresponding to Ce^{+4} $3d_{3/2}$ and Ce^{+4} $3d_{5/2}$ [31]. The Fe $2p_{1/2}$ and Fe $2p_{3/2}$ peaks were also detected at about 723.9 eV and 710.44 eV. The Fe $2p_{3/2}$ can be deconvoluted to two peaks at 712.35 and 710.25 eV with a shakeup satellite, which confirms the presence of both Fe^{3+} and Fe^{2+} in the CDM sample [32].

The specific surface area and porosity of the samples were measured using the N_2 adsorption-desorption and calculated by BET and BJH models. The results showed that the cerium doping had a positive effect on the specific surface area of Fe_3O_4 NPs. Furthermore, $a_{s,BET}$ of bare MAG and ceria increased from 42.113 m^2/g to 51.272 m^2/g and about 50.034 m^2/g, respectively. On the contrary, the $a_{s,BET}$ of mechanically doped ceria- MAG was reduced to 18.353 m^2/g. The detailed data on the BET results are provided in Table S1. As shown in Fig. 3a, the hysteresis loops of all the nanoparticles were H3 type, indicating the multi-layer structure of the NPs, with loose interactions between the adsorbent and adsorbate [33]. In addition, the BJH plots of MAG, CDM, and CDMD are also provided in Fig. S4, and the N_2 adsorption-desorption and the BJH plots of bare ceria is given in Fig. S5.

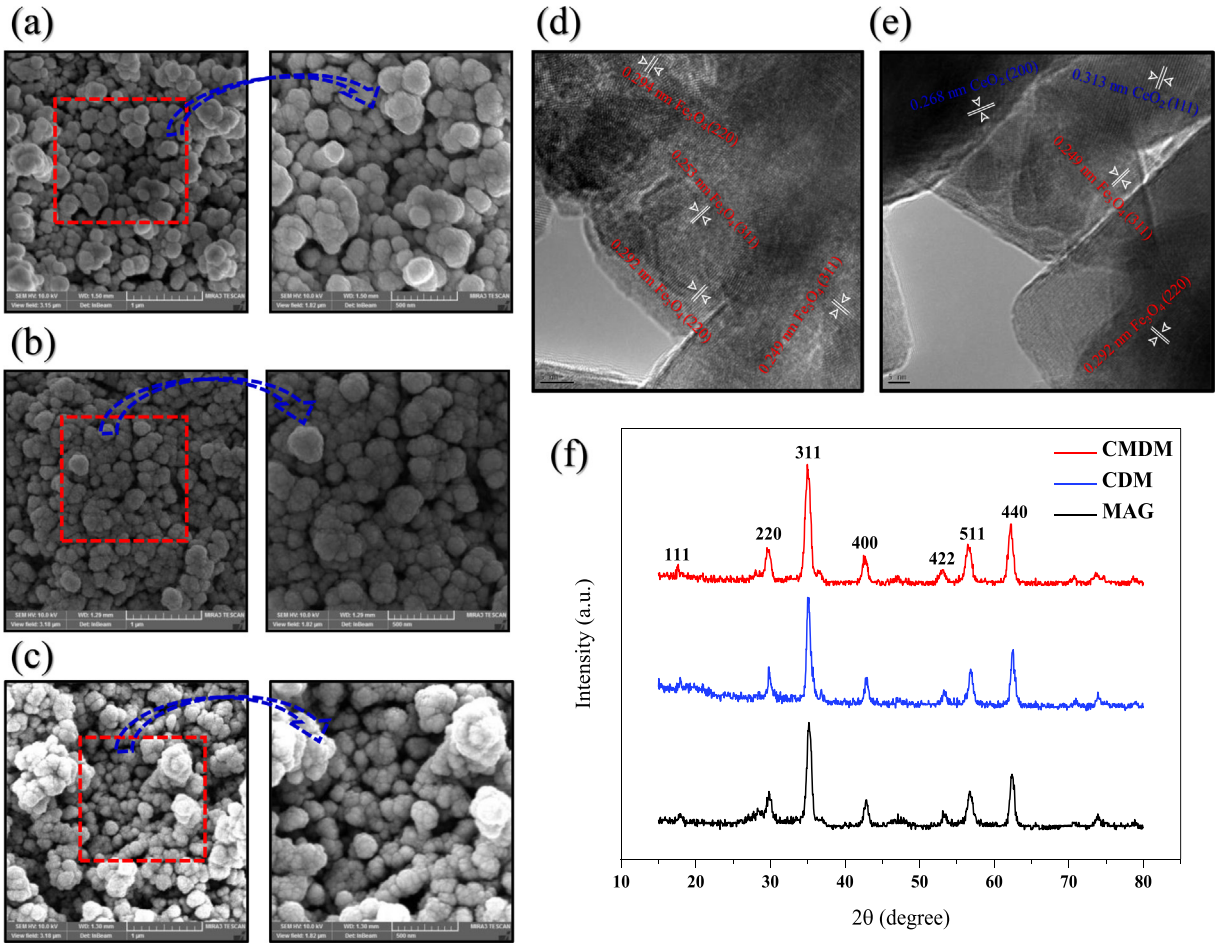

Fig. 1. The FESEM micrographs of (a) MAG NPs, (b) CDM NPs, and (c) CMDM NPs. The HRTEM images of (d) CDM NPs, (e) CMDM NPs, and (f) The XRD pattern of so-synthesized samples.

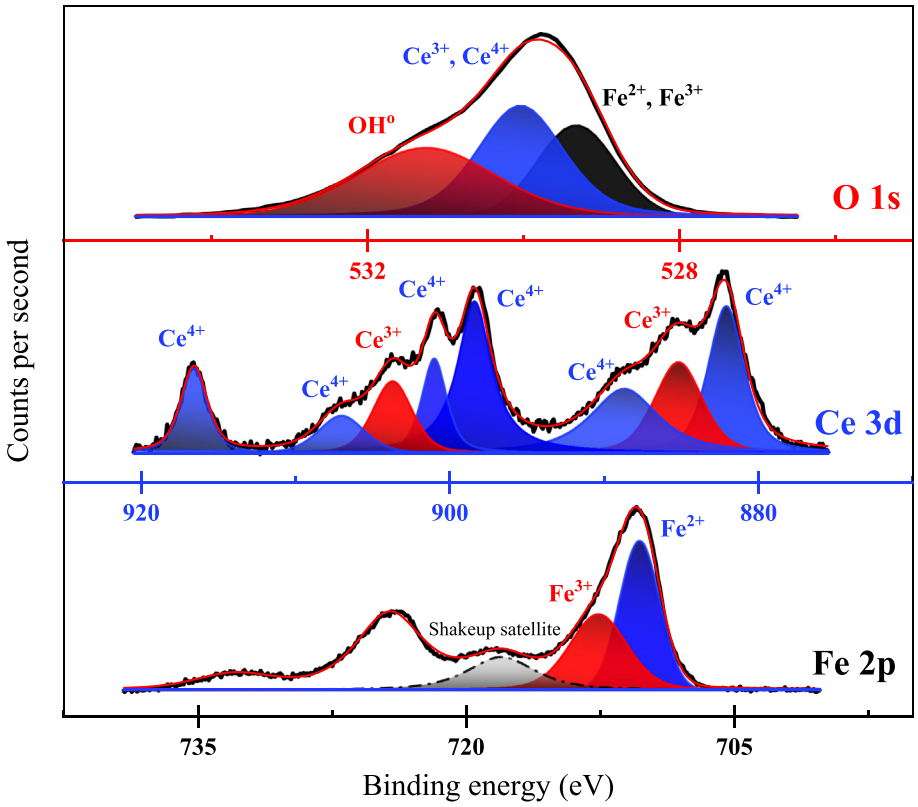

Fig. 2. The HRXPS of CDM samples for O 1 s, Ce 3d, and Fe 2p.

The FTIR analysis was conducted to study the functional groups of nanoparticles and the possible structural impurities. As shown in Fig. 3b, the characteristic peaks of Fe—O bond appeared at about 650 to 680 1/cm in all the samples [34]. The small shift in the CDM and CMDM samples confirmed the successful doping of cerium with magnetite. In the FTR spectra of CDM and CMDM, the characteristic peaks appeared at 494, 542, 649, and 1383 1/cm could be attributed to the stretching vibration of the Ce—O bond [30]. The absorption peaks detected at 3425 and 1634 1/cm corresponds to the adsorbed water molecules. The FTIR spectrum of bare ceria can be seen in Fig. S6.

The magnetic behavior of the samples was studied using vibrating sample magnetometer. The hysteresis loops of "S" shape and small squareness ratios proved the superparamagnetic nature of the synthesized NPs (Fig. 3c, Table S2.). Since the saturation magnetization value of 38.19 emu/g for CDM sample was comparable to that of the bare MAG (*Ms* of 54.58 emu/g), it can be concluded that the doping of cerium doesn't have a great effect on the magnetic behavior of MAG [35].

3.2. Effect of nanoparticles

The CL reaction of luminol-ferricyanide was utilized to study the effect of the prepared NPs. The CL reaction mechanism of the luminol-ferricyanide system has been initially investigated by Shevlin and Neufeld [36]. It was established that the relaxation of the excited state of 3-aminophthalate (3-aminophthalate*) at 425 nm lead to the CL emission. 3-aminophthalate* as a product of luminol oxidation is produced as a result of the reaction of luminol radical and diazaquine with reactive oxygen species (ROS such as $^{\bullet}OH$, $O_2^{\bullet-}$ or the other radical derivatives) [37].

The kinetic profiles (Fig. 4a) and UV–vis absorption spectra (Fig. 4b) were studied to figure out the mechanism of the target CL system. In the absence of the NPs, the CL emission of luminol-$K_3Fe(CN)_6$ was relatively weak in the alkaline medium (Fig. 4a). However, the CL intensity of the system was enhanced about 1.5 times in the presence of CDM, wherein the enhancement effect of CDM was greater than those of MAG, CeO_2,

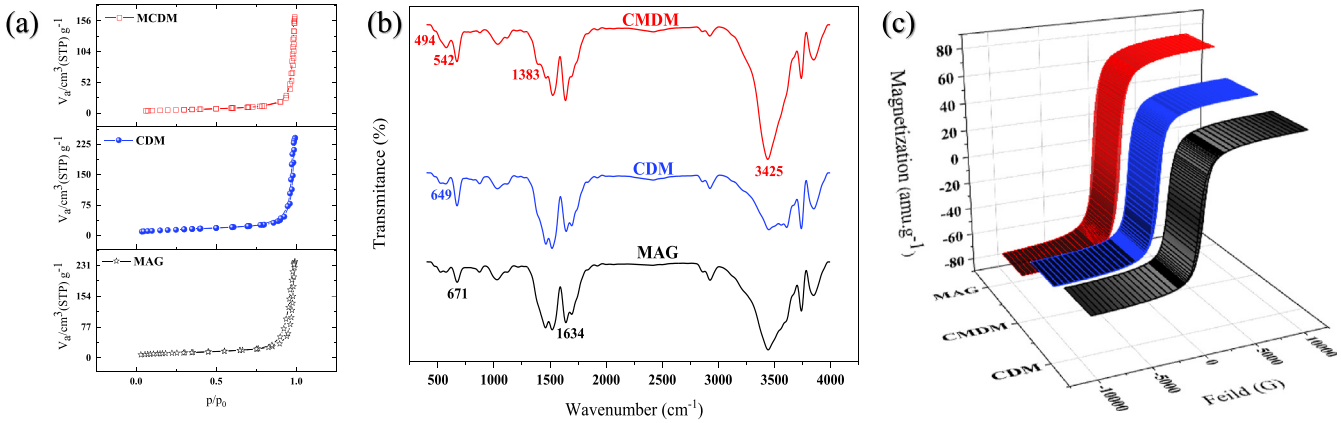

Fig. 3. (a) The BET isotherms of so-synthesized samples, (b) FTIR spectra of so-synthesized samples, and (c) The hysteresis loops of the so-synthesized samples.

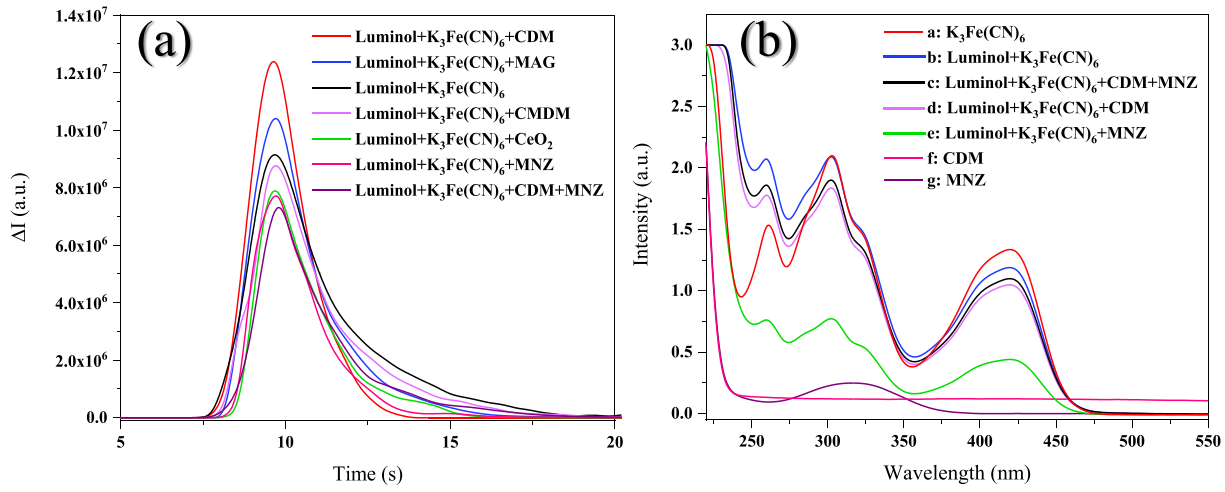

Fig. 4. (a) Kinetic profiles for different CL systems. (b) UV–Vis absorption spectra of luminol- $K_3Fe(CN)_6$-CDM in alkaline media; The concentrations of luminol, $K_3Fe(CN)_6$, NaOH and different catalysts (MAG, CeO_2, CDM, and CMDM) were 10^{-3}, 0.05, 1.5, and 9.52×10^{-5} mol/L, respectively.

and CMDM. Because, as mentioned in the characterization section, the reduction in the CMDM surface area could reduce its enhancing effect. Since the application of CDM could give rise to the generation of reactive oxygen species such as •OH, $O_2^{\bullet -}$, the boosting effect of CDM on CL intensity can be attributed to the formation of $O_2^{\bullet -}$ [38]. Under this condition, the oxidation reaction of luminol was facilitated by $O_2^{\bullet -}$ thus enhancing the CL emission (Scheme 3). In contrast, the application of Fe_3O_4 and CeO_2 had lower effects on CL intensity, thus revealing the interactional contribution of these compartments for the enhanced influence of CDM.

As illustrated in Fig. 4b, ferricyanide has 3 absorption peaks at about 260, 310, and 425 nm (curve a). The maximum absorption peak of MNZ was located at the wavelength of about 315 nm (curve g) and CDM gave rise to a linear absorption peak (curve f). Considering the diminished intensity of the absorption peak of luminol-ferricyanide system (curve b) in the presence of CDM (curve d), it can be concluded that CDM

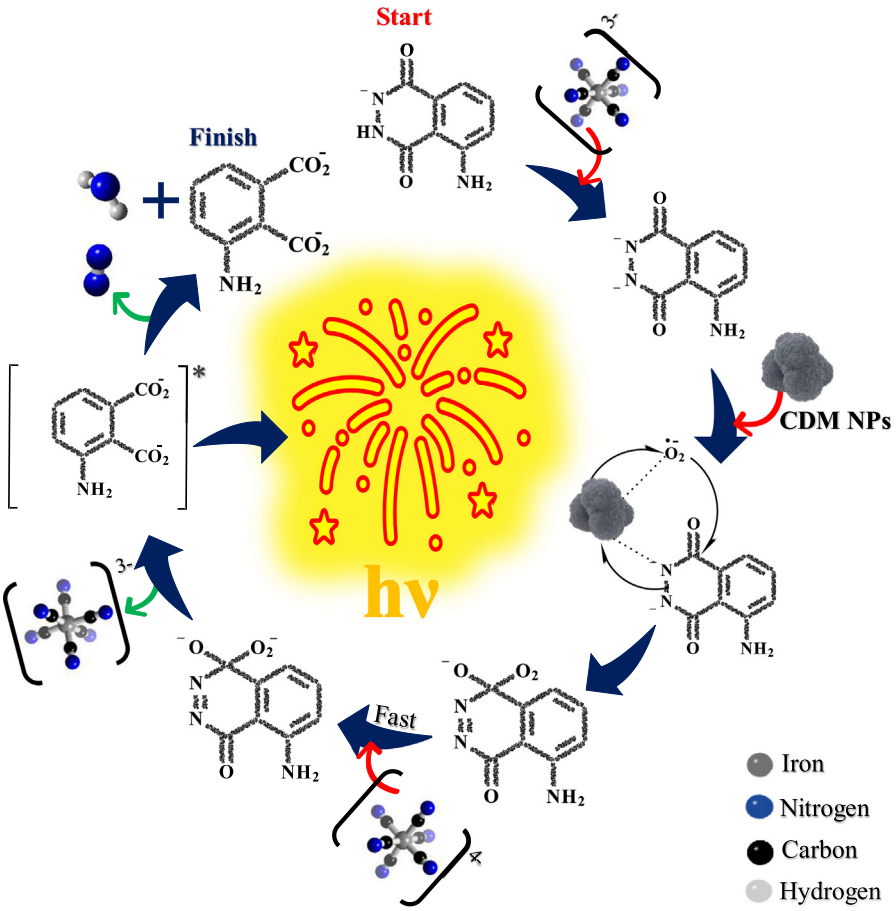

Scheme 3. Schematic illustration of the proposed CL assay for MNZ detection.

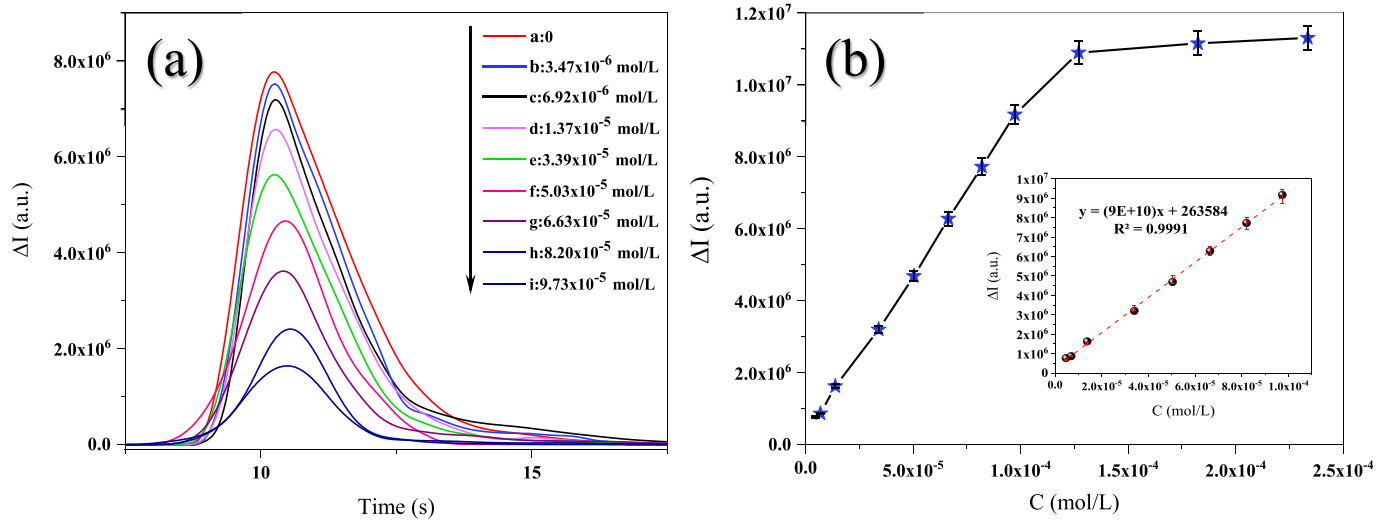

Fig. 5. (a) Kinetic profiles for luminol- $K_3Fe(CN)_6$-CDM CL system after injection of different concentrations of MNZ solution [luminol = 10^{-3} mol/L, NaOH = 1.5 mol/L, $K_3Fe(CN)_6$ = 0.05 mol/L, and CDM = 9.52×10^{-5} mol/L]. (b) Calibration graph for the determination of MNZ, the inset shows the linear part of the calibration graph.

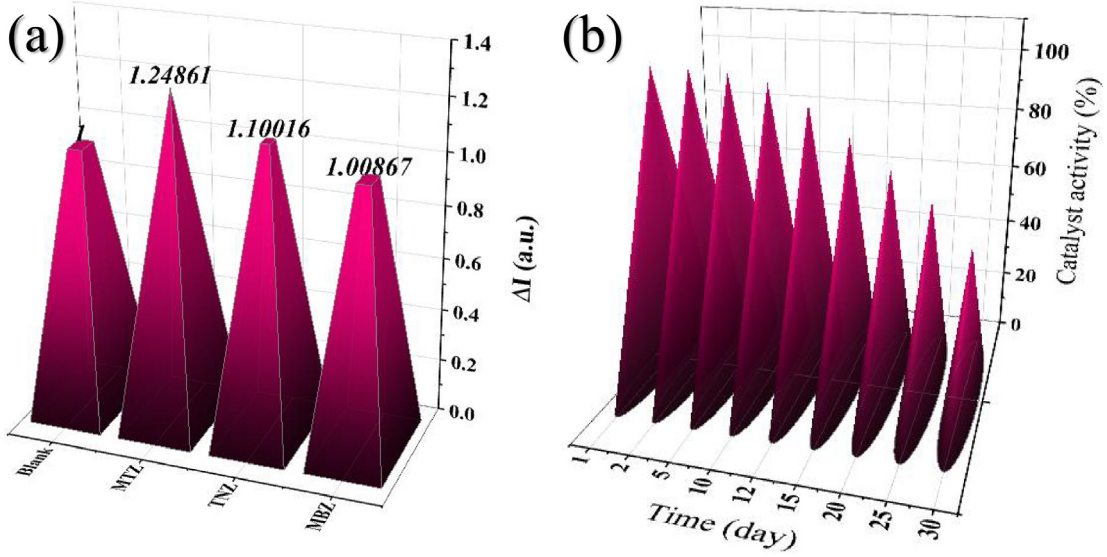

Fig. 6. (a) CL response of luminol- $K_3Fe(CN)_6$-CDM system towards MNZ and its analogues; The concentrations of luminol, $K_3Fe(CN)_6$, NaOH and CDM were 10^{-3}, 0.05, 1.5, and 9.52×10^{-5} mol/L, respectively. (b) Catalytic activity of prepared CDM in certain times after its synthesis.

has had an interaction with the reactants or intermediates in the system. The inhibitory effect of MNZ was also studied on the proposed CL system. The absorbance of luminol-ferricyanide-CDM-MNZ (curve c) system was not equal to those of the two individual systems (curves d and g). This indicates that MNZ could be involved and oxidized in the luminol-ferricyanide-MNZ (curve e) reaction system and resulted in new products. Therefore, the quenching role of MNZ could be derived from a reducing group (e.g. OH). As reported previously [37,39], the

Table 1
Comparison of the purposed method with some methods reported in literature for determination of MNZ.

Method	Catalyst	Matrix	LODs (mg/L)	Linear range (mg/L)	Ref.
Fluorescence	Fluorescent membrane	Human serum	0.360	1.23–35.48	[42]
Fluorescence	GQDs-embedded SMIP[a]	Human serum	0.026	0.034–2.567	[43]
Spectrophotometric	Vanillin and PDAB[b]	Tablet formulations	0.080	10.0–60.0	[44]
Spectrophotometric	–	Pharmaceutical dosage forms and human urine	83.100	5.0–25.0	[45]
SERS[c]	Silver nanorod array	Environmental Samples	10.000	10.0–50.0	[46]
Electrochemical	Nanostructure thin film on the gold electrode	Pharmaceutical and human urine	0.250	0.85–71.0	[47]
Electrochemical	Ni/Fe-LDH	Tablets	9.927	0.85–275.56	[48]
HPLC	–	Human serum	0.040	0.06–10.0	[49]
GC-FID[d]	–	Tablets and ovules	2.500	50.0–6030.0	[50]
CL	$Fi_{2.8}Ce_{0.2}O_4$	Human serum	0.067	0.59–16.66	This work

[a] Graphene quantum dots embedded silica molecularly imprinted polymer.
[b] *P*-dimethyl amino benzaldehyde.
[c] Surface Enhanced Raman Spectroscopy.
[d] Gas Chromatography and Flame Ionization Detector.

Table 2
Interference of different species on the determination of 3×10^{-5} mol/L MNZ (in optimum condition).

Coexisting substance	Tolerance limit (interference to analyte ratio)
Cu^{2+} and Cl^{-}	1000
Na^{+}, Co^{2+}, Mg^{2+}, CH_3COO^{-}, NO_3^{2-}, and SO_4^{2-}	500
Alanine, glucose, lactose, Fe^{2+}, and Zn^{2+}	200
Starch, valine, Ca^{2+}, Ni^{2+}, Pb^{2+}, and CO_3^{2-}	100
K^{+}, Br^{-}, and PO_4^{3-}	50

functional groups of MNZ could react by ROS and prevent their production, leading to the decreased CL intensity. Consequently, the MNZ molecules could cover CDM surface and prevent its catalytic action in the studied CL system.

3.3. Optimization of CL reaction parameters

In order to access the sensitivity of the system for MNZ determination, the CL reaction conditions were optimized. The effects of the influential parameters were investigated in reference to the ΔI value, where $\Delta I = I_0\text{-}I_s$, I_0 is the CL signal in the absence of MNZ, and I_s is the CL signal in the presence of MNZ. The ΔI value revealed the decreased efficacy of MNZ on the emitted CL intensity of luminol-$K_3Fe(CN)_6$-CDM system. The efficacy of some key factors is shown in Fig. S7.

Fig. S7(a and b) shows that the most sensitive CL system was achieved using 10^{-3} mol/L luminol and 1.5 mol/L NaOH. These low quantities could be limited to the kinetic of CL reaction.

The effect of the concentration of ferricyanide solution on ΔI of the CL system was also investigated (Fig. S7c). The optimum concentration of ferricyanide was 0.05 mol/L, which could be attributed to the absorption of the emitted radiation by a strong colored oxidant [40]. The quantity of the cerium used for the synthesis of CDM could also play an important role in its catalytic yield. Accordingly, several NPs were synthesized with different quantities of cerium and applied to the CL system (Fig. S8). The maximum CL intensity was obtained by the CDM sample containing 0.2 of cerium ($Fe_{3-x}Ce_xO_4$, $x = 0.2$). The lower amounts of Ce gave rise to less active CDM samples due to the insignificant active sites. on the other hand, the higher amounts of Ce had negative effect on CDM activity because of the minimized porosity of the synthesized samples. Fig. S7 d shows that the highest CL emission was obtained at 9.52×10^{-5} mol/L of CDM. Notably, once the concentration of nanomaterial increases, strong interactions take place [41]. On this basis, the catalytic efficiency of CDM NPs was decreased in the CL system. Besides, the absorption of the emitted radiation by CDM NPs at higher concentrations could reduce the catalytic performance of the NPs.

3.4. Analytical figures of merit

The CDM ($Fe_{2.8}Ce_{0.2}O_4$) supported CL system was used for the determination of MNZ. The CL intensity was decreased when the high magnitudes of MNZ was used (Fig. 5a). Moreover, a linear relationship was achieved for the concentration range of 3.47×10^{-6} to 9.37×10^{-5} mol/L of MNZ ($\Delta I = (9E{+}10)\ (C_{MNZ}) + 263{,}584$, $R^2 = 0.9991$) (Fig. 5b). The limit of detection (LOD) was also 3.91×10^{-7} mol/L.

Table 4
Results for the determination of MNZ in spiked environmental water samples.

Sample	Added (mol/L)	Found (CL method) (mol/L)	Recovery (%)
Water	0	–	–
Tap water	1.75×10^{-6}	1.63×10^{-6}	93.14
	3.50×10^{-6}	3.56×10^{-6}	101.71
River water	5.84×10^{-6}	5.66×10^{-6}	96.91
	1.75×10^{-5}	1.72×10^{-5}	98.28

Furthermore, the CL sensor was tested for the detection of some other drugs including tinidazole (TNZ) and mebendazole (MBZ) and the results are shown in Fig. 6a. The studies revealed that the compounds with a chemical structure similar to MNZ could also quench the CL intensity owing to the existence of the same functional group on them. This outcome indicated the sensitivity of the suggested CL tool for the detection of the same group of drugs, in particular MNZ. The analytical properties of different approaches were compared to those of the investigated CL system in this study (Table 1). This comparison shows that the fabricated CL method in this study provides a relatively good sensitivity and it can be used for detection of MNZ and its analogues owing to its reliability and promptness.

The precision of the studied system was also investigated by measuring 10^{-5} and 3×10^{-5} mol/L of MNZ solution, for 5 times. The relative standard deviation (%) was 1.94% and 3.33%, respectively. Moreover, the CL solution offered good stability during the study (Fig. 6b).

3.5. Selectivity

The selectivity of the developed sensor was investigated by measuring a constant concentration of MNZ (3×10^{-5} mol/L) in the presence of various ionic species and intervening compounds with different concentrations. An interfering effect of <5% on the signal of MNZ was presumed as the tolerance limit (Table 2). Most of the studied compounds demonstrated insignificant effects on the MNZ determination results. Besides, for further elimination of the intervening compound efficacies, a dilution ratio of 1:500 of the original samples was very helpful.

3.6. Analysis of real samples

The applicability of the proposed system for real samples was assessed through MNZ determination in human serum and spiked water samples. The studied samples were supplied and examined based on the procedures outlined in the experimental subdivision. The obtained results were then compared with corresponding values

Table 5
Results for the determination of MNZ in pharmaceutical formulation.

Nominal (mg/vial)	Official method (mg/vial)	Proposed CL method (mg/vial)	t-Statistic[a]
10	10.17	10.23	1.79

[a] t-Critical = 4.30 for $n = 6$ and $P \geq .05$.

Table 3
Results for the determination of MNZ in human plasma.

QC sample	Added concentration of drug in plasma (mol/L)	Found concentration of drug in plasma (mol/L)	Mean recovery (%)	CV (%)[a]	Accuracy	n[b]
Low	6.92×10^{-6}	6.94×10^{-6}	100.36	2.57	98.11	6
Medium	3.39×10^{-5}	3.34×10^{-5}	98.57	5.19	94.82	6
High	8.20×10^{-5}	8.15×10^{-5}	99.43	2.44	105.68	6

[a] Coefficient of variation.
[b] Number of determinations.

obtained from HPLC as an official method and the differences were evaluated by the Student *t*-test. Tables 3 and 4 present the results obtained for the human serum and spiked water samples, respectively. The accuracy and applicability of the proposed system were approved based on the results obtained from a set of recovery experiments for samples' solutions. From the results provided in Table 5, the difference between the results of the employed was found to be insignificant.

4. Conclusion

We have reported a CL assay based on the catalytic activity of cerium doped magnetite in the luminol-$K_3Fe(CN)_6$ CL system with the quenching effect of MNZ, which could effectively detect MNZ. Excellent selectivity, high sensitivity, and simplicity of this approach were the main advantages of which can be emphasized. The detection limit of 3.91×10^{-7} mol/L was achieved with this approach in the linear range of 3.47×10^{-6}-9.37×10^{-5} mol/L, which has not been reported so far. More importantly, this sensor was applicable to detect MNZ in intricate mediums such as plasma. Hence, the application of this sensor in various areas including biological and medical diagnostics is strongly expected.

Declaration of competing interest

We would like to confirm that there is no known conflict of interest associated with this publication.

Acknowledgment

The authors are thankful to the University of Tabriz for the support provided. This work is funded by Nanjing Forestry University [Grant nos. 163020139, 163040109 and 163020236] and the grant no. NRF-2019R1A5A8080290 of the National Research Foundation of Korea.

Appendix A. Supplementary data

Supplementary data to this article can be found online at https://doi.org/10.1016/j.saa.2020.118272.

References

[1] S.K. Arya, C.C. Wong, Y.J. Jeon, T. Bansal, M.K. Park, Advances in complementary-metal–oxide–semiconductor-based integrated biosensor arrays, Chem. Rev. 115 (2015) 5116–5158, https://doi.org/10.1021/cr500554n.
[2] B. Vahid, J. Hassanzadeh, B. Khodakarami, CdSe quantum dots-sensitized chemiluminescence system and quenching effect of gold nanoclusters for cyanide detection, Spectrochim. Acta A Mol. Biomol. Spectrosc. 212 (2019) 322–329, https://doi.org/10.1016/j.saa.2019.01.017.
[3] J. Motoyoshiya, J. Wada, K. Itoh, K. Wakabayashi, T. Maruyama, K. Ono, K. Fukasawa, T. Fujimoto, Y. Akaiwa, E. Nonaka, Fluorescence and chemiluminescence behavior of distyrylbenzene bearing two arms of dipicolylaminomethyl groups: interactions with zinc ion and ATP, Acta. A. Mol. Biomol. Spectrosc. 195 (2018) 223–229, https://doi.org/10.1016/j.saa.2018.01.059.
[4] Z. Gu, A. Fu, L. Ye, K. Kuerban, Y. Wang, Z. Cao, Ultrasensitive chemiluminescence biosensor for nuclease and bacterial determination based on Hemin-encapsulated Mesoporous silica nanoparticles, ACS Sens 4 (2019) 2922–2929, https://doi.org/10.1021/acssensors.9b01303.
[5] F. Ejeian, P. Etedali, H.-A. Mansouri-Tehrani, A. Soozanipour, Z.-X. Low, M. Asadni, A. Taheri-Kafrani, A. Razmjou, Biosens. Bioelectron. 118 (2018) 66–79.
[6] R.A. Petros, J.M. DeSimone, Strategies in the design of nanoparticles for therapeutic applications, Nat. Rev. Drug Discov. 9 (2010) 615–627, https://doi.org/10.1038/nrd2591.
[7] Y. Alhamoud, D. Yang, S.S. Fiati Kenston, G. Liu, L. Liu, H. Zhou, F. Ahmed, J. Zhao, Advances in biosensors for the detection of ochratoxin a: bio-receptors, nanomaterials, and their applications, Biosens. Bioelectron. 141 (2019), 111418. https://doi.org/10.1016/j.bios.2019.111418.
[8] A. Chen, S. Chatterjee, Nanomaterials based electrochemical sensors for biomedical applications, Chem. Soc. Rev. 42 (2013) 5425–5438, https://doi.org/10.1039/C3CS35518G.
[9] K.P. McKenna, F. Hofer, D. Gilks, V.K. Lazarov, C. Chen, Z. Wang, Y. Ikuhara, Atomic-scale structure and properties of highly stable antiphase boundary defects in Fe_3O_4, Nat. Commun. 5 (2014) 5740, https://doi.org/10.1038/ncomms6740.
[10] Y. Sun, J. Li, Y. Wang, C. Ding, Y. Lin, W. Sun, C. Luo, A chemiluminescence biosensor based on the adsorption recognition function between Fe_3O_4@SiO_2@GO polymers and DNA for ultrasensitive detection of DNA, Spectrochim. Acta A Mol. Biomol. Spectrosc. 178 (2017) 1–7, https://doi.org/10.1016/j.saa.2017.01.057.
[11] H. He, Y. Zhong, X. Liang, W. Tan, J. Zhu, C. Yan Wang, Natural magnetite: an efficient catalyst for the degradation of organic contaminant, Sci. Rep. 5 (2015), 10139. https://doi.org/10.1038/srep10139.
[12] G.G. Gerent, A. Spinelli, Magnetite-platinum nanoparticles-modified glassy carbon electrode as electrochemical detector for nitrophenol isomers, J. Hazard. Mater. 330 (2017) 105–115, https://doi.org/10.1016/j.jhazmat.2017.02.002.
[13] G. Guan, L. Yang, Q. Mei, K. Zhang, Z. Zhang, M.-Y. Han, Chemiluminescence switching on peroxidase-like Fe_3O_4 nanoparticles for selective detection and simultaneous determination of various pesticides, Anal. Chem. 84 (2012) 9492–9497, https://doi.org/10.1021/ac302341b.
[14] L. Shen, C. Chu, C. Ma, H. Yang, S. Ge, J. Yu, M. Yan, X. Song, An ultrasensitive quenched electrochemiluminescent immunoassay based on the peroxidase-like activity of $ZnFe_2O_4$@Au nanoparticles, Sens. Actuators B Chem. 201 (2014) 196–203, https://doi.org/10.1016/j.snb.2014.05.002.
[15] H. Duan, L. Li, X. Wang, Y. Wang, J. Li, C. Luo, A sensitive and selective chemiluminescence sensor for the determination of dopamine based on silanized magnetic graphene oxide-molecularly imprinted polymer, Spectrochim. Acta A Mol. Biomol. Spectrosc. 139 (2015) 374–379, https://doi.org/10.1016/j.saa.2014.12.051.
[16] S. He, W. Shi, X. Zhang, ,J. Li, Y. Huang, β—Cyclodextrins-based inclusion complexes of $CoFe_2O$ magnetic nanoparticles as catalyst for the luminol chemiluminescence system and their applications in hydrogen peroxide detection, Talanta. 82 (2010) 377–383. doi:https://doi.org/10.1016/j.talanta.2010.04.055.
[17] H. Peng, G. Liu, X. Dong, J. Wang, W. Yu, J. Xu, Magnetic, luminescent and core–shell structured Fe_3O_4@YF_3:Ce^{3+},Tb^{3+} bifunctional nanocomposites, Powder Technol. 215–216 (2012) 242–246, https://doi.org/10.1016/j.powtec.2011.10.006.
[18] H. Peng, G. Liu, X. Dong, J. Wang, J. Xu, W. Yu, Preparation and characteristics of Fe_3O_4@YVO_4:Eu^{3+} bifunctional magnetic–luminescent nanocomposites, J. Alloys Compd. 509 (2011) 6930–6934, https://doi.org/10.1016/j.jallcom.2011.04.004.
[19] C.R. De Silva, S. Smith, I. Shim, J. Pyun, T. Gutu, J. Jiao, Z. Zheng, Lanthanide(III)-doped magnetite nanoparticles, J. Am. Chem. Soc. 131 (2009) 6336–6337, https://doi.org/10.1021/ja9014277.
[20] H. Liu, C. Di Valentin, Shaping magnetite nanoparticles from first principles, Phys. Rev. Lett. 123 (2019), 186101. https://doi.org/10.1103/PhysRevLett.123.186101.
[21] T.S. Rad, A. Khataee, S. Rahim Pouran, Synergistic enhancement in photocatalytic performance of Ce (IV) and Cr (III) co-substituted magnetite nanoparticles loaded on reduced graphene oxide sheets, J. Colloid Interface Sci. 528 (2018) 248–262, https://doi.org/10.1016/j.jcis.2018.05.087.
[22] D. Kim, H.J. Kwon, T. Hyeon, Magnetite/ceria nanoparticle assemblies for extracorporeal cleansing of amyloid-β in Alzheimer's disease, Adv. Mater. 31 (2019), 1807965. https://doi.org/10.1002/adma.201807965.
[23] V. Singh, R. Nerimetla, M. Yang, S. Krishnan, Magnetite-quantum dot Immunoarray for plasmon-coupled-fluorescence imaging of blood insulin and glycated hemoglobin, ACS Sens 2 (2017) 909–915, https://doi.org/10.1021/acssensors.7b00124.
[24] M. Mohammad, A. Razmjou, K. Liang, M. Asadnia, V. Chen, Metal–organic-framework-based enzymatic microfluidic biosensor via surface patterning and biomineralization, ACS Appl. Mater. Interfaces 11 (2019) 1807–1820.
[25] Y. Gu, X. Yan, C. Li, B. Zheng, Y. Li, W. Liu, Z. Zhang, M. Yang, Biomimetic sensor based on molecularly imprinted polymer with nitroreductase-like activity for metronidazole detection, Biosens. Bioelectron. 77 (2016) 393–399, https://doi.org/10.1016/j.bios.2015.09.060.
[26] R. Hassandoost, S.R. Pouran, A. Khataee, Y. Orooji, S.W. Joo, Hierarchically structured ternary heterojunctions based on Ce^{3+}/ Ce^{4+} modified Fe_3O_4 nanoparticles anchored onto graphene oxide sheets as magnetic visible-light-active photocatalysts for decontamination of oxytetracycline, J. Hazard. Mater. 376 (2019) 200–211, https://doi.org/10.1016/j.jhazmat.2019.05.035.
[27] B. Tanhaei, A. Ayati, M. Lahtinen, M. Sillanpää, Preparation and characterization of a novel chitosan/Al_2O_3/magnetite nanoparticles composite adsorbent for kinetic, thermodynamic and isotherm studies of methyl orange adsorption, Chem. Eng. J. 259 (2015) 1–10, https://doi.org/10.1016/j.cej.2014.07.109.
[28] Z. Chen, M. Wang, C. Zhao, Y. Lin, R. Yang, Z. Wang, Shape-controlled synthesis of Fe_3O_4/CeO_2 hybrid octahedra for lipase immobilization, CrystEngComm 17 (2015) 2536–2543.
[29] Y. Cao, L. Wen, F. Svec, T. Tan, Y. Lv, Magnetic AuNP@Fe_3O_4 nanoparticles as reusable carriers for reversible enzyme immobilization, Chem. Eng. J. 286 (2016) 272–281, https://doi.org/10.1016/j.cej.2015.10.075.
[30] M.E. Khan, M.M. Khan, M.H. Cho, Ce^{3+}-ion, surface oxygen vacancy, and visible light-induced photocatalytic dye degradation and photocapacitive performance of CeO_2 graphene nanostructures, Sci. Rep. 7 (2017) 5928.
[31] X. Liu, J.R. Ray, C.W. Neil, Q. Li, Y.-S. Jun, Enhanced colloidal stability of CeO_2 nanoparticles by ferrous ions: adsorption, redox reaction, and surface precipitation, Environ. Sci. Technol. 49 (2015) 5476–5483.
[32] W. Zhao, C. Liang, B. Wang, S. Xing, Enhanced photocatalytic and Fenton-like performance of CuO_x-decorated $ZnFe_2O_4$, ACS Appl. Mater. Interfaces 9 (2017) 41927–41936.
[33] A. Mohammadi, S.E. Moosavifard, A. Goljanian Tabrizi, M.M. Abdi, G. Karimi, Nanoporous $CuCo_2S_4$ microspheres: a novel positive electrode for high-performance hybrid energy storage devices, ACS Appl. Energy Mater. 2 (2019) 627–635, https://doi.org/10.1021/acsaem.8b01651.
[34] X. Zhang, L. Chen, R. Liu, D. Li, X. Ge, G. Ge, The role of the OH Group in citric acid in the coordination with Fe_3O_4 nanoparticles, Langmuir 35 (2019) 8325–8332, https://doi.org/10.1021/acs.langmuir.9b00208.

[35] C. Chingakham, A. David, V. Sajith, Fe_3O_4 nanoparticles impregnated eggshell as a novel catalyst for enhanced biodiesel production, Chin. J. Chem. Eng. (2019) https://doi.org/10.1016/j.cjche.2019.02.022.
[36] P.B. Shevlin, H.A. Neufeld, Mechanism of the ferricyanide-catalyzed chemiluminescence of luminol, J. Org. Chem. 35 (1970) 2178–2182.
[37] Q. Li, L. Zhang, J. Li, C. Lu, Nanomaterial-amplified chemiluminescence systems and their applications in bioassays, TrAC Trends Anal. Chem. 30 (2011) 401–413, https://doi.org/10.1016/j.trac.2010.11.008.
[38] M. Haddad Irani-nezhad, A. Khataee, J. Hassanzadeh, Y. Orooji, A chemiluminescent method for the detection of H_2O_2 and glucose based on intrinsic peroxidase-like activity of WS2 quantum dots, Molecules 24 (2019) 689.
[39] A. Safavi, G. Absalan, F. Bamdad, Effect of gold nanoparticle as a novel nanocatalyst on luminol–hydrazine chemiluminescence system and its analytical application, Anal. Chim. Acta 610 (2008) 243–248, https://doi.org/10.1016/j.aca.2008.01.053.
[40] H. Liu, Y. Hao, J. Ren, P. He, Y. Fang, Determination of tsumacide residues in vegetable samples using a flow-injection chemiluminescence method, Lumin. J. Biol. Chem. Lumin. 22 (2007) 302–308.
[41] A.R. Khataee, A. Hasanzadeh, M. Iranifam, M. Fathinia, Y. Hanifehpour, S.W. Joo, CuO nanosheets-enhanced flow-injection chemiluminescence system for determination of vancomycin in water, pharmaceutical and human serum, Spectrochim. Acta A Mol. Biomol. Spectrosc. 122 (2014) 737–743, https://doi.org/10.1016/j.saa.2013.12.014.
[42] A. Muhammad, T. Muhammad, O. Yimit, B. Yakup, Novel fluorescent membrane for metronidazole sensing prepared by covalent immobilization of a pyrenebutyric acid derivative, J. Fluoresc. 23 (2013) 599–604.
[43] M. Mehrzad-Samarin, F. Faridbod, A.S. Dezfuli, M.R. Ganjali, A novel metronidazole fluorescent nanosensor based on graphene quantum dots embedded silica molecularly imprinted polymer, Biosens. Bioelectron. 92 (2017) 618–623, https://doi.org/10.1016/j.bios.2016.10.047.
[44] K. Siddappa, M. Mallikarjun, P.T. Reddy, M. Tambe, Spectrophotometric determination of metronidazole through Schiff's base system using vanillin and PDAB reagents in pharmaceutical preparations, Eclética Quím 33 (2008) 41–46.
[45] M.M. Issa, A.M.A. Shanab, N.T. Shaat, Kinetic spectrophotometric H-point standard addition method for the simultaneous determination of diloxanide furoate and metronidazole in binary mixtures and biological fluids, Spectrochim. Acta A Mol. Biomol. Spectrosc. 114 (2013) 592–598.
[46] C. Han, J. Chen, X. Wu, Y. Huang, Y. Zhao, Detection of metronidazole and ronidazole from environmental samples by surface enhanced Raman spectroscopy, Talanta 128 (2014) 293–298.
[47] B. Rezaei, S. Damiri, Fabrication of a nanostructure thin film on the gold electrode using continuous pulsed-potential technique and its application for the electrocatalytic determination of metronidazole, Electrochim. Acta 55 (2010) 1801–1808.
[48] K. Nejati, K. Asadpour-Zeynali, Electrochemical synthesis of nickel–iron layered double hydroxide: application as a novel modified electrode in electrocatalytic reduction of metronidazole, Mater. Sci. Eng. C. 35 (2014) 179–184.
[49] T.G. Do Nascimento, E. de Jesus Oliveira, R.O. Macêdo, Simultaneous determination of ranitidine and metronidazole in human plasma using high performance liquid chromatography with diode array detection, J. Pharm. Biomed. Anal. 37 (2005) 777–783.
[50] S. Ashour, N. Kattan, Simultaneous determination of miconazole nitrate and metronidazole in different pharmaceutical dosage forms by gas chromatography and flame ionization detector (GC-FID), Int. J. Biomed. Sci. IJBS. 6 (2010) 13.